Paper No. 180

ISMS 2016

Quantitative evaluation of stope damage induced by seismic waves

Atsushi Sainoki *, Hani S. Mitri

Department of Mining and Materials Engineering, McGill University, Montreal, Canada, H3A 0E8

ABSTRACT
In the present study, a methodology to evaluate damage around underground openings due to seismic waves arising from mining-induced fault-slip is proposed. First, expressions for an associated flow rule with a failure criterion developed for biaxial stress conditions are derived, which are newly implemented into FLAC3D code. With the code, stope extraction is simulated using a 3D mine-wide model encompassing a fault running parallel to a steeply dipping orebody. The failure criterion for biaxial stress conditions is applied to only the rockmass in the vicinity of stopes within the hanging wall. After extracting stopes in the orebody, mining-induced fault-slip is simulated in dynamic conditions, considering its trigger mechanism, i.e., stress drop caused by instantaneous shearing of fault surface asperities, using Barton's shear strength model. Damage to the rockmass caused by seismic waves is then evaluated with the increase in plastic strain. The proposed methodology takes into account the mechanism of mining-induced fault-slip, propagation of seismic waves, biaxial stress conditions on the surface of openings, and plastic strain as damage criterion.
KEYWORDS: stability of mine opening; mining-induced fault-slip; seismic waves; biaxial stress condition

1. INTRODUCTION

Stress redistribution caused by mining activities, such as stope extraction, can lead to the reactivation of pre-existing faults. As a result, fault-slip can occur, producing seismic waves. When the seismic waves hit underground openings, rockbursts could take place. Thus, in order to ensure a safe working environment and stable production, it is paramount to understand the mechanism of mining-induced fault-slip and elucidate the relation between the seismic waves and the damage to mine openings.

It is common that the numerical modelling of mining-induced fault-slip is conducted with the conventional Mohr-Coulomb failure criterion in static conditions (Hofmann and Scheepers, 2011). Importantly, the method does not replicate the actual mechanism of mining-induced fault-slip. In reality, the surface of faults in underground mines is undulating and has asperities that interlock with each other. Instantaneous stress drop caused by the shearing of such asperities, which is related to the occurrence of mining-induced fault-slip, cannot be accurately modelled with the conventional method. Furthermore, the numerical analysis in static conditions is incapable of producing seismic waves arising from fault-slip; hence it is impossible to evaluate damage to nearby mine openings inflicted by the seismic waves.

Recently, Sainoki and Mitri (2014a) have developed the methodology to simulate mining-induced fault-slip with Barton's shear strength model (Barton, 1973) in dynamic conditions, considering the stress drop induced by asperity shear. The methodology is capable of modelling mining-induced fault-slip in a more robust way than the use of the Mohr-Coulomb failure criterion. Furthermore, as the analysis is performed in dynamic conditions, the propagation of seismic waves can be simulated. Although a number of studies have been undertaken about the effect of seismic waves on the stability of an underground opening, studies especially focused on the effect of seismic waves arising from mining-induced fault-slip have not been undertaken sufficiently. Recently, Wang and Cai (2015) examine the effect of seismic waves on an excavation while considering a point source of a fault-slip event, but the magnitude of fault-slip is an input parameter, that is, it fails to estimate damage induced by fault-slip that could take place under the ambient stress state.

Another important aspect to be considered is that a failure criterion around an opening where stress state is biaxial. It has been demonstrated that the consideration to the intermediate stress is required (Yun et al., 2010) in order to predict the failure of rock under biaxial stress conditions, where spalling resulting from extension fractures is expected (Diederichs, 2007). Due to the difficulty of considering or implementing failure criteria for such biaxial stress conditions, to the author's knowledge, such failure criteria have never been applied in the numerical modelling of underground openings.

In light of a literature review, the present study is focused on estimating the damage around an underground opening induced by seismic waves

*Corresponding author – email: atsushi.sainoki@mail.mcgill.ca

arising from mining-induced fault-slip whilst considering the failure of rockmass under biaxial stress conditions. The fault-slip is modelled in static and dynamic conditions whilst considering the asperity shear as its source mechanism, and damage induced by the seismic waves to a stope in a deep hard rock mine is evaluated whilst taking into account the failure under biaxial stress conditions.

2. METHODOLOGY

2.1 Constitutive model for fault

As discussed in the introduction, the effect of fault surface asperities is taken into consideration with the Barton's shear strength model (Barton 1973), which is expressed as follows:

$$\tau_{\max} = \sigma_n \tan\left[JRC\log_{10}\left(\frac{JCS}{\sigma_n}\right) + \phi_b\right] \tag{1}$$

where $\tau_{\max}$ and σ_n are the maximum shear strength and the normal stress acting on a fault; and JRC, JCS and ϕ are joint roughness coefficient, joint wall compressive strength, and friction angle, respectively. Comparison of Barton's shear strength model with the classical Mohr-Coulomb model is shown in Figure 1. As can be seen in the figure, the shear strength calculated from Barton's model is invariably greater than that from the Mohr-Coulomb model.

Barton's shear strength model is implemented into the ubiquitous joint model of FLAC3D (Itasca, 2009). The implementation procedure is based on the plastic flow rule, i.e., the increment of plastic strain is determined with the derivative of potential function with respect to its stress components and a scalar variable derived from the consistency condition. The detailed procedure of the implementation is provided in Sainoki and Mitri (2014a). In order to simulate fault-slip triggered by the shearing of fault surface asperities, JRC is instantaneously decreased during a dynamic analysis, which is described in more detail later.

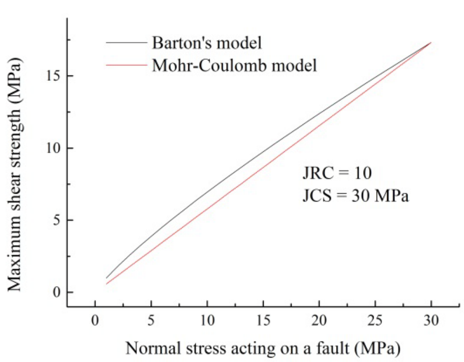

Figure 1: Barton's shear strength model.

2.2 Failure criterion under biaxial stress state and its implementation to FLAC3D

Yun et al. (2010) perform biaxial tests for several types of rock and establish a failure criterion under biaxial stress conditions, which are the stress conditions that take place on the surface of underground openings. The failure criterion is expressed as follows:

$$\frac{\sigma_1}{\sigma_c} = A + B\frac{\sigma_2}{\sigma_c} + C\left(\frac{\sigma_2}{\sigma_c}\right)^2 \tag{2}$$

where σ_1, σ_2 and σ_c are the maximum compressive stress, intermediate stress and uniaxial compressive strength (UCS), respectively; and *A*, *B*, and *C* are material constants. In order to implement the equation as a yield criterion into FLAC3D, compression needs to be defined as a negative quantity and the equation is multiplied by UCS, consequently giving the following equation:

$$F = \sigma_1 + A\sigma_c - B\sigma_2 + C\frac{(\sigma_2)^2}{\sigma_c} \tag{3}$$

Note that compression has a negative quantity in Equation (3). Following the same procedure shown in Sainoki and Mitri (2014a), the scalar variable that determines plastic strain increments is expressed as follows:

$$\lambda = \frac{\{\partial F/\partial \boldsymbol{\sigma}\}^T [D]\{\Delta\boldsymbol{\varepsilon}\}}{\{\partial F/\partial \boldsymbol{\sigma}\}^T [D]\{\partial g/\partial \boldsymbol{\sigma}\}} \tag{4}$$

where [D] is an elastic matrix that relates strain with stress, and $\Delta\boldsymbol{\varepsilon}$ is a strain increment vector. In the present study, an associated flow rule is assumed. The derivatives of the yield function with respect to each stress component are as follows:

$$\frac{\partial F}{\partial \sigma_1} = 1 \tag{5}$$

$$\frac{\partial F}{\partial \sigma_2} = -B + 2C\frac{\sigma_2}{\sigma_c} \tag{6}$$

$$\frac{\partial F}{\partial \sigma_3} = 0 \tag{7}$$

Then, the increments of plastic strain follow the plastic flow rule as follows:

$$\{\Delta\boldsymbol{\varepsilon}^p\} = \lambda\left\{\frac{\partial g}{\partial(\boldsymbol{\sigma})}\right\} \tag{8}$$

where $\Delta\boldsymbol{\varepsilon}^p$ is a plastic strain increment vector, and g is plastic potential. As the plastic strain increments do not contribute to the stress increments, the stress correction to be made at each step during the iterative analysis of FLAC 3D is expressed as follows:

$$\{\Delta\boldsymbol{\sigma}\} = -\lambda[D]\left\{\frac{\partial g}{\partial(\boldsymbol{\sigma})}\right\} \tag{9}$$

Figure 2 shows the failure criterion of granite under biaxial stress conditions derived from regression analysis (Yun et al. 2010). The material constants, *A*, *B*, and *C* in Equation (3) are 0.998, 1.873, and -1.533, respectively. The present study uses the material constant of granite, although the rock type to which the failure criterion is applied is norite. Both norite and granite are hard rocks.

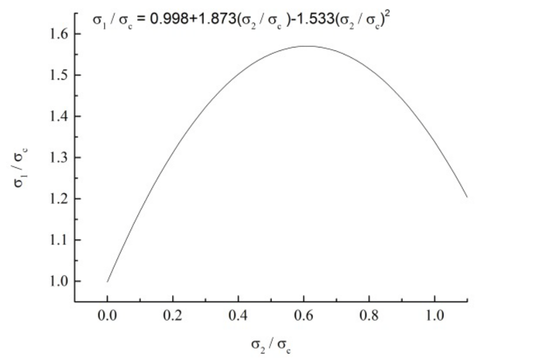

Figure 2: Failure criterion of granite under biaxial stress conditions.

2.3 Numerical model description

The present study focuses on an underground mine with a fault running parallel to a steeply dipping, tabular orebody. Such tabular orebodies are frequently encountered in hard rock mines in Canada and are extracted with sublevel stoping methods (Zhang and Mitri, 2008). Figure 3 depicts a numerical model encompassing such geological structures. As can be seen in the figure, the height, width, and length of the model are 300 m, 332 m, and 300 m, respectively. The dimensions are basically the same as that analyzed by Sainoki and Mitri (2014a), who determined that the effect of the external boundaries on the stress state around the orebody and the fault is negligible. The fault runs parallel to the orebody and steeply dips at 80˚. Dense meshes are generated near the orebody and the fault in order to simulate stress re-distribution caused by mining activities as accurately as possible, while mesh density decreases towards the model outer boundaries. The total numbers of zones and grid points in the model are 215040 and 230643, respectively.

Stopes are modelled in the orebody and extracted according to the mining sequence as per sublevel stoping method with delayed backfill. Figure 4 shows stope dimensions and the mining sequence. It can be seen from the figure that each sublevel contains two stopes. In total, 18 stopes are designed. The mining sequence starts from the bottom and proceeds upwards. For each sublevel, the stopes on the hanging wall side are extracted first. As for dimensions of the stopes, the height is 30 m and the strike length is 200 m as shown in Figure 4(a) and (b), respectively. As a large amount of extraction of orebody induces regional stress re-distribution that eventually triggers fault-slip, such long stope strike length is adopted rather than extracting numerous stopes on each level. Note that the stopes are backfilled immediately after the extraction.

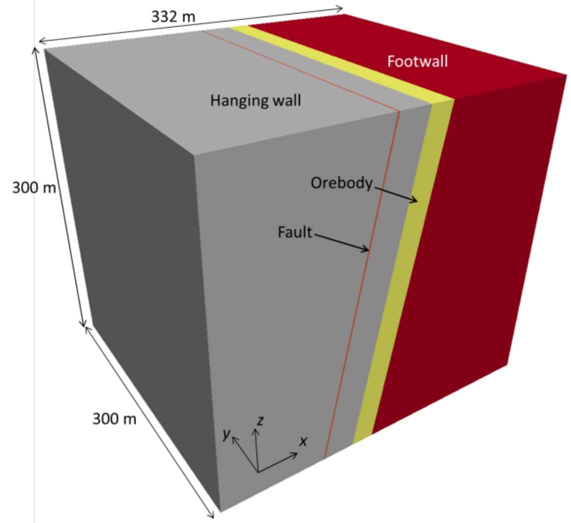

Figure 3: Isometric view of numerical model analyzed encompassing a fault running parallel to the orebody.

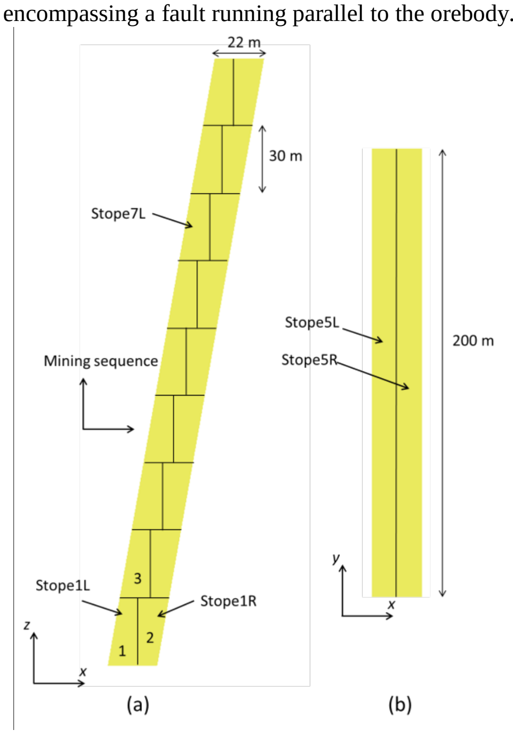

Figure 4: Stopes modelled within the orebody and mining sequence as per sublevel stoping method: (a) cross-section, (b) plan view at z = 150 m.

2.4 Analysis procedure

First, static analyses are performed, in which the stopes in the orebody are extracted and backfilled in accordance with the mining sequence after simulating in-situ stress state. The stope extraction is continued until Stope7L, at which point the fault is adequately unclamped, consequently increasing potential for fault-slip sufficiently as shown in the study (Sainoki and Mitri, 2014b). Subsequently, based on the stress state after extracting stope7L, dynamic analysis is conducted. At the beginning of the dynamic analysis, the boundary condition is changed to viscous in order to prevent seismic waves arising from fault-slip from reflecting on the boundaries. At the same time, the stress state on the fault is examined, and then for the area where plastic shear movements are taking place along the fault, the JRC and friction angle of the fault are decreased, thereby inducing an instantaneous stress drop that drives fault-slip. The decrease in JRC represents shearing of fault surface asperities, while the reduction in friction angle denotes the transition from static to kinetic friction. At each step during the dynamic analysis, the stress state on the fault is checked and the change in the mechanical properties is performed if the conditions are satisfied. In this way, fault-slip is driven during the dynamic analysis.

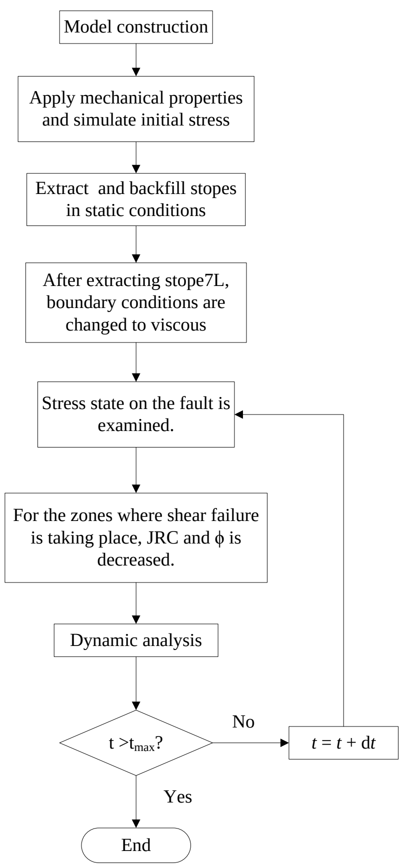

Figure 5: Analysis procedure for static and dynamic analyses.

2.5 Mechanical properties of rockmass and fault

Mechanical properties of the rockmasses are derived from the case study (Henning, 1998). According to the study, rock types for the hanging wall, orebody, and footwall are rhyolite tuff, massive sulphide, and rhyolite, respectively, and the mechanical properties estimated from laboratory experiments are converted to those for rockmasses with the rockmass rating system proposed by (Bieniawski, 1989). Table 1 lists deformation modulus, E, cohesive strength, C, friction angle, ϕ, unit weight, γ, tensile strength, σ_T, and dilation angle, ψ. Note that the tensile strength is assumed to be one-tenth of the uniaxial compressive strength calculated from the cohesion and friction angle (Tesarik et al., 2003) and the dilation angle is assumed to be one-fourth of the friction angle (Hoek and Brown, 1997) except that for the backfill (Traina, 1983).

Table 1: Mechanical properties of rockmass and backfill.

	Hanging wall	Ore	Footwall	Backfill
E (GPa)	31	115	49	2.5
C(MPa)	2.6	11.5	4.3	0.1
ϕ (˚)	38	48	39	35
γ (kN/m^3)	25.5	25.5	25.5	23.0
σ_T (MPa)	1.1	5.9	1.8	0.3
ψ ( )	9.3	12.0	9.5	0.0

The mechanical properties of the fault that are applied to the ubiquitous joint model are listed in Table 2. The modulus of elasticity is set to one-tenth that of the hanging wall. According to Barton and Choubey (1977), basic friction angles of typical rocks range from 21˚ to 38˚. The adopted value is an intermediate value of the range. Likewise, typically, JRC ranges from 0 to 20 (Barton, 1973), thus giving the intermediate value of 10. Regarding the dynamic friction angle, ϕ_d, the same value as that used by Sainoki and Mitri (2014a) is applied. It should be noted that the dynamic friction angle is applied to zones where the shear stress acting on the fault reaches the maximum shear strength during the dynamic analysis.

Table 2: Mechanical properties of a fault.

E (GPa)	ϕ (˚)	JRC	ϕ_d (˚)	γ (kN/m^3)
3.1	30	10	15	25.5

Regarding the material constants in Equation (2), the influence of geological conditions is taken into account with RMR (Bieniawski, 1989). Specifically, the equation proposed by Mirti (1994) is applied to B and C. As a result, the two parameters, B, and C, are decreased to 0.79, and -0.65, respectively. Regarding parameter A, it remains the same because UCS in the equation is directly decreased with the Hoek-Brown parameter s (Hoek and Brown, 1997).

3. RESULTS AND DISCUSSION

Figure 6 shows the particle velocity (PV) of grid points during the dynamic analysis in the sectional view at y = 150 m as well as the extent of fault-slip on the fault 0.4 s after the onset of the analysis. Note that the white-colored region in the figure is Stope7L. The propagation of seismic waves arising from the fault-slip can be clearly seen from the figure. Figure 6(a) shows PV after 0.01 s. It is found that extremely high PV exceeding 1 m/s takes place in the vicinity of the fault. As time goes by, regions with relatively high PV move away from the fault, indicating the propagation of seismic waves. After 0.04 s, ground motion occurs in extensive regions as a result of the wave propagation. At the same time, the maximum PV in the section decreases to 0.5 m due to wave attenuation. Note that the present study adopts the local damping system embedded in FLAC3D, assuming a local damping coefficient of 5 %.

Comparison of PV amongst the different stages suggests that the most intensive PV takes place near the stope after 0.02 s. Afterwards, the magnitude of PV near the stope continuously decreases due to the wave attenuation and propagation. Thus, the damage induced by the seismic waves is evaluated at the stage, i.e., 0.02 s after the onset of dynamic analysis.

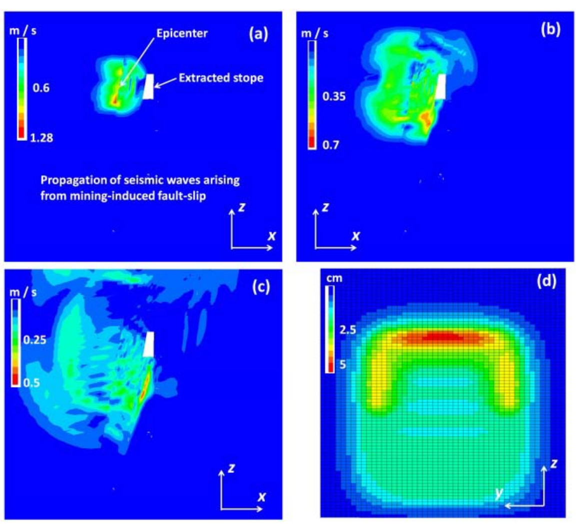

Figure 6: Particle velocity (PV) in the sectional view of the model at y = 150 m: (a) 0.01 s after the onset of the dynamic analysis, (b) 0.02 s, (c) 0.04 s, and (d) extent of fault-slip on the fault after 0.04 s.

In the present study, damage to the rockmasses is evaluated with the ratio of plastic strain to elastic strain as shown in Figure 7. The quantity or its variations are widely employed to evaluate damage. For instance, its inverse is used as the elastic damage model (Zhu et al., 2014).

Figure 8 shows damage induced solely by the seismic waves arising from fault-slip, i.e., damage due to the plastic strain induced by the extraction of stope is subtracted. It is interesting that damage does not increase uniformly in the region between the stope and the fault. For instance, a noticeable increase in damage can be observed within the following three locations: backfill under the stope, the hanging wall, and the upper part of the stope. Detailed discussion on the reason why the discrepancy in damage occurs is not made in the present study, but it is speculated that the concentration of damage is attributed to the state of stress before the fault-slip takes place and PV at the moment when the damage is computed. Hence, the distribution of damage might change at some degree if the damage is computed at different elapsed time. Note that emphasis should be placed on the developed methodology to evaluate damage induced by seismic waves quantitatively that considers the mechanism of mining-induced fault-slip.

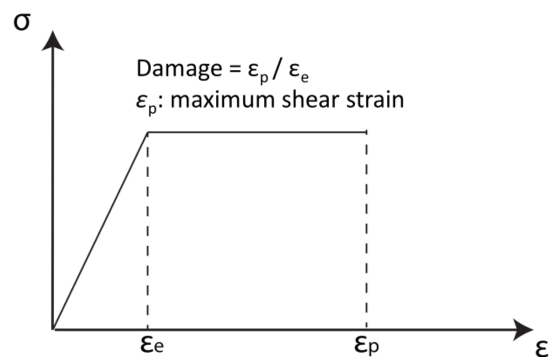

Figure 7: Schematic illustration to show damage calculation.

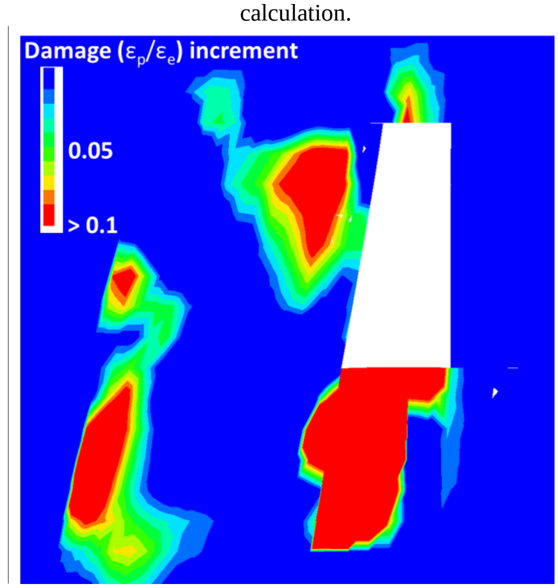

Figure 8: Damage induced by seismic waves.

4. CONCLUSIONS

The present study proposes a methodology to evaluate damage induced by seismic waves arising from fault-slip. In order to replicate the actual mechanism of mining-induced fault-slip, the effect of fault surface asperities is taken into account, whereby fault-slip is driven in dynamic conditions by an instantaneous stress drop due to the shearing of the asperities. The dynamic analysis enables the observation of the propagation of seismic waves, i.e., particle velocity, at given elapsed time after the onset of fault-slip. A methodology to evaluate damage induced by the seismic waves is proposed. It is then demonstrated that damage does not distribute uniformly around the stope. The proposed methodology helps to identify locations where noticeable damage takes place and to estimate the severity of the damage.

5. ACKNOWLEDGEMENT

This work is financially supported by a grant by the Natural Science and Engineering Research Council of Canada (NSERC) in partnership with Vale Ltd – Sudbury Operations, Canada, under the Collaborative Research and Development Program. The authors are grateful for their support.

6. REFERENCES

Barton, N. (1973). Review of a new shear-strength criterion for rock joints Engineering Geology, Volume 7, pp. 287-332

Barton, N., & Choubey, V. (1977). The shear strength of rock joints in theory and practice. Rock Mechanics, Volume 10, pp. 1-54

Bieniawski, Z. T. (1989). Engineering rock mass classifications. New York: Wiley.

Diederichs, M.S. (2007). The 2003 Canadian Geotechnical Colloquium: Mechanistic interpretation and practical application of damage and spalling prediction criteria for deep tunnelling. Canadian Geotechnial Journal, Volume 44, pp. 1082-1116.

Henning, J. (1998). Ground control strategies at the bousquet 2 mine. (Master), McGill University, Montreal, QC, Canada.

Hoek, E. (2007). Practical rock engineering.

Hoek, E., & Brown, E.T. (1997). Practical estimates of rock mass strength. International Journal of Rock Mechanics and Mining Science, Volume 34, No. 8, pp. 1165-1186.

Hofmann, G.F., & Scheepers, L.J. (2011). Simulating fault slip areas of mining induced seismic tremors using static boundary element numerical modelling. Mining Technology, Volume 120, No. 1, pp. 53-64.

Itasca. (2009). FLAC3D - fast Lagrangian analysis of continua (Version 4.0). U.S.A.: Itasca Consulting Group Inc.

Mitri, H.S., Edrissi, R., & Henning, J. (1994). Finite element modelling of cable-bolted stopes in hardrock ground mines. Paper presented at the SME Annual Meeting, Albuquerque, New Mexico.

Sainoki, A., & Mitri, H.S. (2014a). Dynamic modelling of fault slip with Barton's shear strength model. International Journal of Rock Mechanics and Mining Science, Volume 67, pp. 155-163

Sainoki, A., & Mitri, H. (2014b). Evaluation of fault-slip potential due to shearing of fault asperities. Canadian Geotechnial Journal, Volume 52, No. 10, pp. 1417-1425.

Tesarik, D.R., Seymour, J.B., & Yanske, T.R. (2003). Post-failure behaviour of two mine pillars confined with backfill. International Journal of Rock Mechanics and Mining Science, Volume 40, No. 2, pp. 221.

Traina, L.A. (1983). Experimental stress-strain behaviour of a low strength concrete under multiaxial states of stress. Kirtland Air Force Base, NM: Air Force Weapons Laboratory.

Wang, X., & Cai, M. (2015). Influence of wavelength-to-excavation span ratio on ground motion around deep underground excavation. Tunnelling and Underground Space Technology, Volume 49, pp. 438-453.

Yun, X., Mitri, H.S., Yang, X., & Wang, Y. (2010). Experimental investigation into biaxial compressive strength of granite. International Journal of Rock Mechanics and Mining Science, Volume 47, pp. 334-341.

Zhang, Y., & Mitri, H. (2008). Elastoplastic stability analysis of mine haulage drift in the vicinity of mined stopes. International Journal of Rock Mechanics and Mining Science, Volume 45, pp. 574-593.

Zhu, W.C., Wei, C.H., Li, S., Wei, J., & Zhang, M.S. (2013). Numerical modeling on destress blasting in coal seam for enhancing gas drainage. International Journal of Rock Mechanics and Mining Science, Volume 59, pp. 179-190.